Journal of Materials Chemistry B



PAPER View Article Online



Cite this: DOI: 10.1039/c9tb00388f

Influence of chemical heterogeneity and microstructure on the corrosion resistance of biodegradable WE43 magnesium alloys

Hesham Mraied,^a Wenbo Wang^b and Wenjun Cai **D***

Magnesium—yttrium-rare earth element alloys such as WE43 are potential candidates for future bioabsorbable orthopedic implant materials due to their biocompatibility, mechanical properties similar to human bone, and the ability to completely degrade *in vivo*. Unfortunately, the high corrosion rate of WE43 Mg alloys in physiological environments and subsequent loss of structural integrity limit the wide applications of these materials. In this study, the effect of chemical heterogeneity and microstructure on the corrosion resistance of two alloys with different metallurgical states was investigated: cast (as in traditional preparation) and as-deposited produced by magnetron sputtering. The corrosion behavior was studied by potentiodynamic polarization and electrochemical impedance spectroscopy tests in blood bank buffered saline solution. It was found that the as-deposited alloy showed more than one order of magnitude reduction in corrosion current density compared to the cast alloy, owing to the elimination of micro-galvanic coupling between the Mg matrix and the precipitates. The microstructure and formation mechanism of corrosion products formed on both alloys were discussed based on immersion tests and direct measurements of X-ray photoelectron spectrometry (XPS) and cross-sectional transmission electron microscopy (TEM) analysis.

Received 26th February 2019, Accepted 20th May 2019

DOI: 10.1039/c9tb00388f

rsc.li/materials-b

1. Introduction

The biodegradable WE43 Mg alloy with major alloying elements of yttrium (Y, 4.1 wt%), neodymium (Nd, 2.1 wt%), and zirconium (Zr, 0.56 wt%) has received much interest lately for potential applications as temporary cardiovascular stents^{1,2} and bone implants.^{3,4} Mg alloys exhibit good cell adhesion in the physiological environment and can safely degrade in the human body; hence no post operation is required once the damaged tissue is healed, minimizing procedure cost and risks.^{5,6} In contrast to conventional medical metallic materials such as titanium, cobalt–chromium, and stainless steel, the mechanical properties of Mg are close to those of human bones,^{7,8} thus minimizing the stress shield effect⁹ and increasing implant stability.⁷ Moreover, Mg is an essential element for human metabolic processes and has been shown to enhance bone growth when used in implants.^{10–12}

Unfortunately, the high degradation rate of Mg alloys in physiological environments^{13,14} and subsequent loss of structural integrity and extensive hydrogen evolution to balance the anodic dissolution^{15,16} limit their wide application. When tested *in vivo*, Witte *et al.*¹⁷ found that the WE43 Mg alloy completely

degraded within 18 weeks. Corrosion of Mg occurs mainly as per the half-cell reactions shown in eqn (1) and (2). The electrons released by the anodic reaction are consumed by the cathodic reaction to generate H_2 gas.¹⁸ The Mg^{2+} and OH^- ions formed by the anodic and cathodic reactions, respectively, will then combine to form a $Mg(OH)_2$ film according to eqn (3):^{19,20}

$$Mg \rightarrow Mg^{2+} + 2e^-$$
 (anodic), (1)

$$2H_2O + 2e^- \rightarrow H_2 + 2OH^- \text{ (cathodic)},$$
 (2)

$$Mg^{2+} + 2OH^{-} \rightarrow Mg(OH)_{2}$$
. (3)

The selection of suitable alloying elements with specific composition is a common approach to enhance the mechanical properties and corrosion resistance of Mg,²¹ as reflected in the composition of the WE43 Mg alloy. The addition of Y promotes precipitation strengthening.^{21,22} In combination with other rare earth elements Y also enhances the creep resistance.²¹ Nd was found to be biocompatible^{23,24} and effective in enhancing the corrosion resistance of Mg alloys by reducing micro-galvanic effects due to the presence of intermetallic compounds.^{25–27} Nd also enhances the mechanical properties of Mg by forming intermetallic phases at the grain boundaries.^{25,28,29} Zr addition increases the strength of Mg mainly by grain refinement.¹² Due to the limited solubility of Zr in Mg, the undissolved Zr particles act as selective nucleation sites during solidification. The corrosion

^a Department of Civil and Environmental Engineering, University of South Florida, 4202 E Fowler Avenue, Tampa, FL 33620, USA

b Department of Materials Science and Engineering, Virginia Polytechnic Institute and State University, Blacksburg, VA 24060, USA. E-mail: caiw@vt.edu

resistance of Mg was found to be enhanced when the concentration of Zr is kept below 2%.21

While alloying is a convenient method to enhance the mechanical properties of Mg, its effect on corrosion resistance is often complicated and detrimental. For example, most Mg alloys exhibit corrosion rates much higher than that of high purity Mg.30 This is because the formation of precipitates and secondary phases often leads to undesired micro-galvanic coupling between the precipitates and the α-Mg matrix, considered to be a dominating corrosion mechanism of Mg alloys. For precipitate-containing Mg alloys, corrosion of the Mg matrix often dominates the overall corrosion behavior of the alloy. Since most (although not all³¹) precipitates are nobler than the Mg matrix, the latter normally serves as a micro-anode and the precipitates as cathodes. Thus the size and distribution of precipitates might affect the precipitate-matrix galvanic coupling and hence control the corrosion rate. In this work, to evaluate the effects of precipitates on the corrosion rate of WE43, corrosion study was performed on WE43 of two metallurgical states: cast and as-deposited. The commercially produced cast samples contain extensive precipitates due to limited solubility of alloying elements in Mg, hence representing a microstructure with a high level of chemical heterogeneity. The deposited samples, prepared using a non-equilibrium processing technique (i.e., physical vapor deposition), contain supersaturated solid solution of all elements, hence representing a microstructure nearly without chemical heterogeneity. Corrosion testing, in situ image monitoring, and post-corrosion microstructure characterization were combined to determine the roles of chemical heterogeneity and microstructure in the corrosion mechanism of the alloy in a simulated physiological environment.

2. Materials and methods

2.1. Materials synthesis

Cast WE43 Mg sheets (1 mm thickness) and sputtering targets with the same global composition of 4.1 wt% Y, 2.1 wt% Nd, 0.56 wt% Zr, and balance Mg were obtained from AEM Products. The cast sheets were cut into several $25 \times 15 \text{ mm}^2$ rectangles for the electrochemical tests. Prior to corrosion testing, the cast samples were mechanically polished using a series of SiC abrasive papers down to 2400 grit size, followed by 0.3 µm alumina polish suspension (Pace Technologies), rinsed with di-water, and air dried. The thin film samples were prepared by DC magnetron sputtering (CRC-100 sputter coater) on (100) Si wafers. Prior to sputtering, the Si wafers were chemically etched using hydrofluoric acid to remove the native oxide film. Sputtering was conducted inside a vacuum chamber (5 mTorr working pressure) with an argon atmosphere at 100 µA current for 3 h to achieve a nominal film thickness of \sim 570 nm.

2.2. Microstructure characterization

The microstructure of cast and as-deposited (hereafter referred to as CT- and AD-WE43) samples was studied by grazing incidence X-ray diffraction (GIXRD, X'Pert PANalytical), using Cu Kα (1.5404 Å) radiation at 40 kV and 40 mA. Data were

collected over 2θ values of $20-80^{\circ}$, 0.015° step size, and 3.5 s per step. The diffraction patterns were then analyzed using X'Pert Highscore software. The surface morphology and composition were characterized using scanning electron microscopy (SEM, Hitachi SU-70) and calibrated energy-dispersive X-ray spectroscopy (EDS, EDAX-Phoenix). EDS analysis was carried out using an acceleration voltage of 10 kV. Transmission electron microscopy (TEM) analysis of AD-WE43 samples, including brightfield (BF) imaging, dark-field (DF) imaging, and selected area diffraction (SAD), was performed using a (Tecani F20) TEM operated at 200 kV. Plane view TEM samples of AD-WE43 samples were prepared by directly sputtering the alloy on continuous carbon film TEM grids for 15 min, which resulted in a sample thickness of ~ 150 nm. Cross-sectional TEM samples of AD-WE43 samples were prepared by using a focused ion beam microscope (FIB, Quanta 200 3D Dual Beam) on the as-deposited AD-WE43 sample using standard lift-out methods. Prior to the lift-out, a carbon protective layer (~ 500 nm) was e-beam deposited, followed by an ion-beam deposited Pt layer ($\sim 1-2$ microns).

2.3. Electrochemical tests

An effective area of 1 cm² of all samples was obtained by using a Gamry PortHole[™] electrochemical sample mask for the electrochemical tests. All electrochemical measurements were performed at room temperature (21 \pm 2 °C) using a Gamry Reference $600^{\text{(R)}}$ potentiostat with the conventional three electrode configuration in naturally aerated and stagnant blood bank buffered saline (BBBS) having a pH of 7.0-7.2 and composition (in g L-1) NaCl: 8.5, Na₂HPO₄: 1.67 and Na₂HPO₄: 0.39. The sample, mixed metal oxide coated titanium mesh, and a commercial silver-silver chloride electrode (1 M KCl internal solution) were used as the working, counter, and reference electrodes, respectively.

Potentiodynamic polarization (PD) measurements were conducted in a single upward scan at a constant scan rate of 1 mV s⁻¹, starting from a cathodic potential (~150 mV below the open circuit potential $E_{\rm OC}$) to an anodic potential (~300 mV above $E_{\rm OC}$). Electrochemical impedance spectroscopy (EIS) tests of all samples were conducted after 15 min of immersion in the electrolyte at $E_{\rm OC}$ in the frequency range of 100 kHz to 100 mHz, 5 points per decade, and 10 mV rms sinusoidal potential excitation. The EIS data were then fitted using Gamry E-chem software. The evolution of H2 gas during the immersion test was measured for both samples during an exposure period of 24 h using an experimental setup shown in Fig. 7(a). The BBBS volume to specimen's surface area ratio of 30 ml cm⁻² was used for both samples and the immersion solution was renewed every 8 h to avoid pH increase due to hydroxide formation.^{32,33} All exposures were conducted at room temperature. All results reported hereafter correspond to the average from at least three separate samples under each test condition. Variability is reported here and for the other observations in this paper as the range of the replicate test results.

2.4. Corrosion product characterization

The post corrosion surface and cross-sections of samples were characterized using scanning electron microscopy (SEM, Hitachi SU-70) and calibrated energy-dispersive X-ray spectroscopy (EDS, EDAX-Phoenix). The cross-sectional samples were prepared by using a focused ion beam microscope (FIB, Quanta 200 3D Dual Beam) operated at 20 kV using Ga ions. The chemical state analysis of corroded samples was conducted by X-ray photoelectron spectroscopy (XPS, PerkinElmer 5100) using an Al K α radiation source at a constant pass energy of 89.45 eV, a step size of 0.5 eV and 10 total sweeps. Transmission electron microscopy (TEM) analysis and EDS line scans were performed on sample cross-sections after electrochemical tests, using a Tecani F20 TEM operated at 200 kV. The TEM samples were prepared by FIB using standard lift-out methods. Prior to the lift-out, a carbon protective layer (\sim 500 nm) was e-beam deposited, followed by an ion-beam deposited Pt layer (\sim 1–2 microns), on the sample surface to protect the outermost (corroded) surface from ion beam damage during FIB.

3. Results and discussion

3.1. Microstructure characterization

Fig. 1(a) shows the surface morphology and the corresponding EDS element maps of CT-WE43. The microstructure consists of a solid solution of the α -Mg matrix and randomly distributed intermetallic precipitates with high Y, Nd, and Zr content, ³⁴ which were formed during solidification. These precipitates have three different shapes: longitudinal, cuboidal, and spherical, as indicated in Fig. 1(a). The average length of the longitudinal

precipitates is 22.0 \pm 3.0 μ m, while the average size of the cuboidal and the spherical particles is 3.5 \pm 0.5 and 6.0 \pm 0.7 μ m, respectively. EDS element maps in Fig. 1(a) show that the longitudinal and spherical precipitates are rich in Nd while the cuboidal particles are rich in both Y and Zr. Table 1 summarizes the compositions of these precipitates. It can be seen that the longitudinal and spherical phases have higher Nd concentration, while the cuboidal phase showed enriched Y and Zr concentration. These findings agree with those of Liu *et al.*, 35 who found that the longitudinal, cuboidal, and spherical phases are enriched in Nd, Y, and Zr, respectively.

The surface morphology of AD-WE43 (Fig. 1(b)) exhibited dense faceted angular structures, which are often associated with the formation of a nanocrystalline phase having columnar through thickness grains. ³⁶ The EDS analysis in Table 1 suggested that the global composition of AD-WE43 is very close to that of CT-WE43. The corresponding EDS element maps in Fig. 1(b) indicated that all alloying elements are homogeneously distributed within the α -Mg matrix, without detectable precipitation at the EDS resolution limit (\sim 200 nm).

Fig. 2 shows the XRD results of both alloys. In CT-WE43, phases corresponding to α -Mg as well as Mg₄₁Nd₅ and Mg₂₄Y₅ precipitates were observed. While the current XRD database does not include results from Mg₂₄(Y,Zr)₅ phases, it is likely that the XRD identified Mg₂₄Y₅ phase also contains Zr, as indicated by prior EDS results (Fig. 1 and Table 1), also reported before.³⁷ On the other hand, only the α -Mg phase was observed

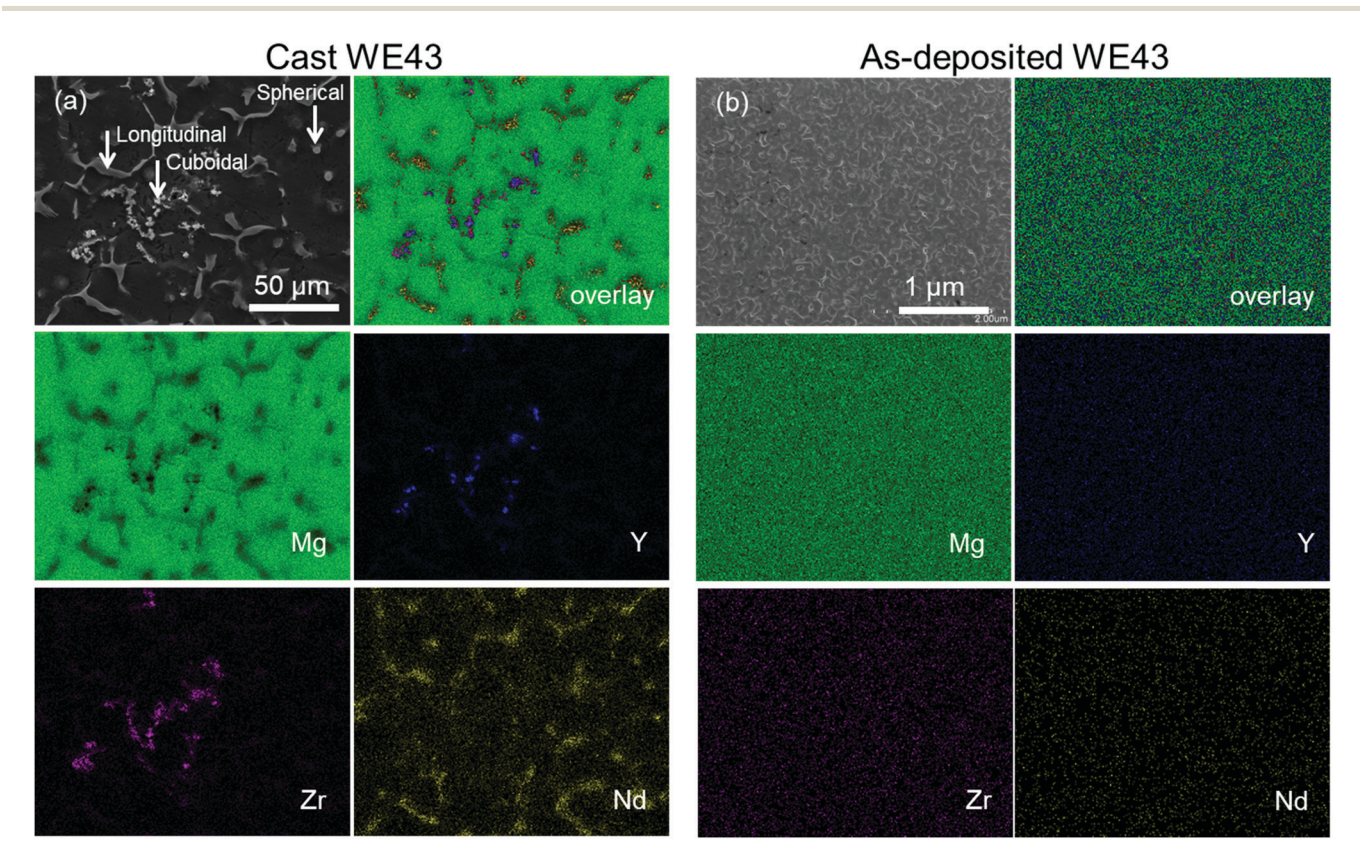


Fig. 1 Surface SEM image and the corresponding EDS element maps of the (a) cast and (b) as-deposited WE43 Mg alloy.

Table 1 Summary of the global and precipitate compositions of cast and as-deposited Mg-WE43, measured by EDS analysis on polished sample surfaces. All values are reported as an average (range)

	Mg (wt%)	Y (wt%)	Nd (wt%)	Zr (wt%)
Cast WE43 (global) Longitudinal/spherical phase Cuboidal phase As-deposited WE43 (global)	69.1 (12.4)	6.6 (6.78) 9.2 (3.8)	7.2 (5.1) 3.5 (3.8)	0.6 (0.4) 3.9 (1.5) 18.1 (7.7) 0.5 (0.2)

in AD-WE43, indicating the supersaturation of Y, Zr, and Nd in the α -Mg matrix. ^{38,39} It is also noted that AD-WE43 exhibited a strong (1120) fiber texture in the film thickness direction, similar to those reported in other PVD deposited Mg alloys. 40 To further characterize the microstructure of AD-WE43, TEM analysis was performed on both plane-view and cross-sectional samples, as shown in Fig. 3. It can be seen that columnar through thickness grains were observed, with an average inplane grain size of 46.6 \pm 12.4 nm, measured using the lineintercept method from multiple DF images. The SAD pattern (Fig. 3(b) inset) exhibited diffraction rings of a single hcp phase, in agreement with the XRD results.

3.2. Potentiodynamic polarization study

Fig. 4 shows representative PD results of both alloys after immersion in BBBS for 20 min. The anodic and cathodic

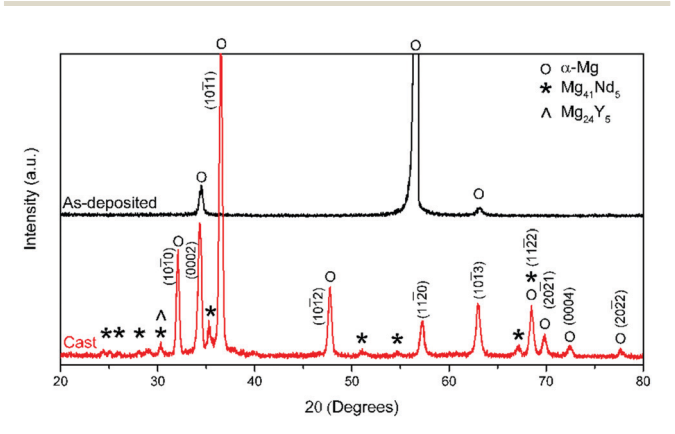


Fig. 2 GIXRD of the cast (red) and as-deposited (black) WE43 Mg alloy

branches of the PD curve are assumed to represent the anodic dissolution of Mg and cathodic hydrogen evolution, respectively. Both alloys showed significant corrosion activity, as is common with Mg alloys. 41 However, it can be seen that AD-WE43 exhibited a shift of both anodic and cathodic branches towards lower corrosion current densities (i_{cor}) , with only a moderate change in the crossover potentials for zero current (E_{zc} , which was close, as expected, to E_{OC}). This pattern indicated a decrease in both anodic and cathodic kinetics of AD-WE43 compared with those of CT-WE43.20,42 This relative trend was clearly reproduced on triplicate testing as illustrated in the inset of Fig. 4. In addition, the anodic branch of CT-WE43 showed very little polarizability, indicative of strongly active dissolution. In contrast, the anodic branch of AD-WE43 showed comparatively modest polarization up to about $-1.4~V_{
m Ag/AgCl}$, suggesting the presence of a somewhat protective film on the alloy surface that breaks down above that potential.8,43

Table 2 lists E_{OC} and the electrochemical parameters obtained from PD tests. The average values of $E_{\rm OC}$ of both alloys were about -1.5 V_{Ag/AgCl}. These values were comparable to those reported elsewhere for the cast WE43 Mg alloy tested at 37 °C in NaCl aqueous solutions (-1.9 to -1.8 $V_{Ag/AgCl}$), simulated body fluids (SBF) $(-1.9 \text{ to } -1.6 \text{ V}_{Ag/AgCl})$ and complete cell culture medium $(-1.7 \text{ to } -1.6 \text{ V}_{Ag/AgCl})$. 3,8,9,44,45 Due to the asymmetry of the anodic and cathodic branches of the PD curves, in this work nominal values of $i_{\rm cor}$ were estimated by Tafel extrapolation of only the cathodic region, using data from potentials that were more than 50 mV more negative than $E_{\rm OC}$. 44,46 As shown in Fig. 4 and Table 2, AD-WE43 exhibited a strong (more than one order of magnitude) reduction in the corrosion current density ($\mu A \text{ cm}^{-2}$), compared to that of CT-WE43. Additional tests (not shown here) of CT-WE43, which included a return scan at an apex potential of -300 mV vs. $E_{\rm OC}$, showed a return loop, indicating the susceptibility of the alloy to localized corrosion. In contrast, those from AD-WE43 revealed no significant hysteresis between the forward and reverse curves. This observation suggested that the chosen scan rate of 1 mV s⁻¹ during PD tests was appropriate for representing the cathodic kinetics used for i_{corr} estimates. It is interesting to note that the i_{corr} values of the as-deposited alloy reported here are remarkably lower than that reported for the plasma ion implanted WE43 Mg alloy in SBF solution. 8,44,47

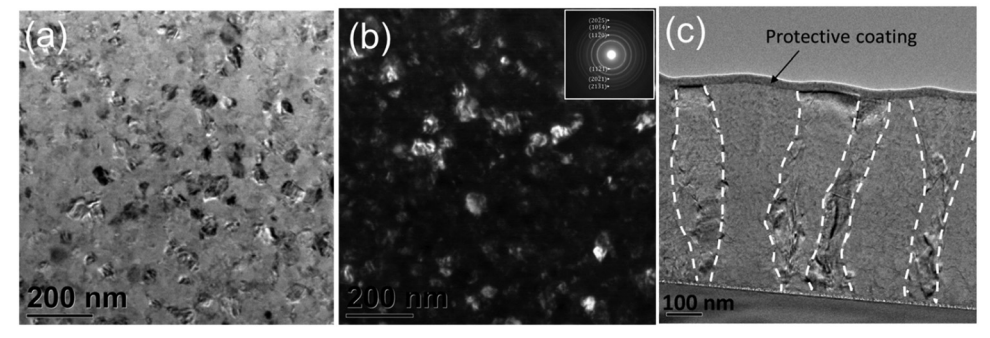


Fig. 3 (a) Bright field (BF) and (b) dark field (DF) TEM images of plane-view samples, and (c) BF TEM image of the cross-sectional sample of the as-deposited WE43 Mg alloy. The inset in (b) shows the corresponding SAD pattern of image (b). Dashed lines in (c) indicate grain boundaries.

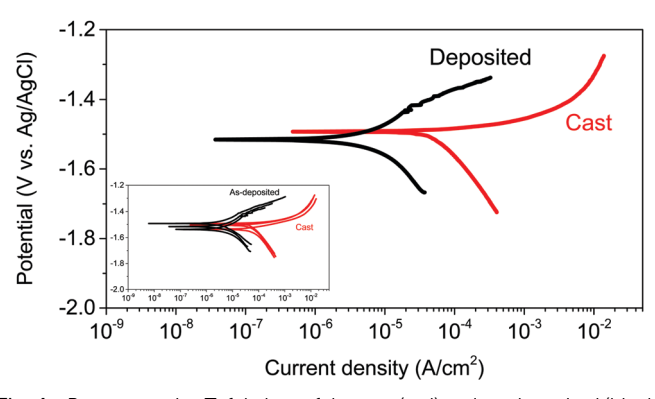


Fig. 4 Representative Tafel plots of the cast (red) and as-deposited (black) WE43 Mg alloy from PD tests after immersion in BBBS for 20 min. The inset shows PD results from three separate tests for each sample set.

3.3. Electrochemical impedance spectroscopy study

To further evaluate the corrosion mechanisms of both alloys, EIS measurements were conducted after E_{OC} stabilization for 15 min in BBBS. Short exposure periods were used on account of the relatively rapid rates of the cast alloy wastage, which might have prevented useful comparison with the deposited alloy at later ages. The Nyquist diagram for representative results is shown in Fig. 5. The diagrams of both alloys were generally similar in having a single capacitive loop shape, comparable with what could be expected from polarization resistance resulting from faradaic processes, coupled with an interfacial charge storage process. Secondary differences, such as a minor inductive component at low frequencies for the cast alloy, may be dismissed as possible artifacts from fast interface evolution during the EIS test run. The experimental data were interpreted using the analog equivalent circuit model shown as the inset in Fig. 5. A constant phase element (CPE) was used instead of a capacitor due to the depression of the Nyquist curve at low frequencies. R_s represents the ohmic solution resistance. In the simplest form, the solution/ metal interface includes polarization resistance (R_P) and a CPE. The Nyquist results showed that both alloys exhibited a similar corrosion mechanism, but the significantly larger capacitive loop of the as-deposited alloy compared to that of the cast alloy indicated an enhanced corrosion resistance3,44 that might be achieved by reducing the chemical heterogeneity.

The impedance of the non-ideal capacitance CPE is represented as

$$Z_{\text{CPE}} = Y_0^{-1} (j\omega)^{-n}, \tag{4}$$

where Y_0 is a constant, $j = (-1)^{1/2}$, ω is the angular frequency and n is a real number between 0 and 1. As shown in Fig. 5, the

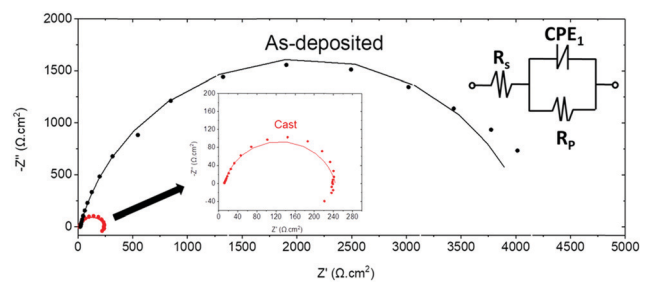


Fig. 5 Representative Nyquist plots (scattered data) of the cast and as-deposited WE43 Mg alloy conducted after $E_{\rm OC}$ stabilization for 15 min in BBBS. The top right inset shows the equivalent circuit model used to fit the experimental data, as represented by the solid lines in the Nyquist plots.

fitted results closely matched the experimental behavior for much of the frequency range for both alloys. It was found that $R_{\rm P}$ for AD-WE43 is 3700 \pm 750 Ω cm², significantly larger than that of the cast alloy (250 \pm 90 Ω cm²), indicating that the former exhibited reduction in the electrochemical reactions occurring at the metal surface, hence enhancing the resistance to Mg dissolution.

The corrosion current density (i_{corr}) from EIS tests was estimated from R_P using the Stern–Geary equation: 41,48

$$i_{\rm corr} = B/R_{\rm P}. \tag{5}$$

 $\it B$ is the apparent Stern–Geary coefficient and can be estimated from

$$B = \frac{\beta_a \cdot \beta_c}{2.3(\beta_a + \beta_c)},\tag{6}$$

where β_a and β_c are the anodic and cathodic Tafel slopes, respectively. It is also noted here that the validity of corrosion current densities estimated from the Stern–Geary equation depends on the correct determination of the coefficient B and whether Mg dissolves directly to Mg²⁺ or through the Mg⁺ intermediate. ^{41,49,50} In this work the value of B was chosen to be equal to 0.026 V, representing the condition of an active metal. As listed in Table 2, the corrosion current density (μ A cm⁻²) of AD-WE43 is much lower (less than 10 times) than that of CT-WE43, in good agreement with the PD tests.

3.4. Immersion test

Results in Sections 3.2 and 3.3 showed that eliminating precipitates in AD-WE43 led to more than one order of magnitude reduction in corrosion current density compared to CT-WE43. To understand the differences in anodic and cathodic reaction kinetics during corrosion of both alloys, $E_{\rm OC}$ and hydrogen (H₂) bubble evolution during the immersion test are presented in Fig. 6 and 7.

Table 2 Electrochemical parameters obtained from PD and EIS tests of the cast and as-deposited WE43 alloy. All values are reported as an average (range)

Samples	$E_{ m OC}$ (mV vs. Ag/AgCl)	$\beta_{\rm c}$ (mV per decade)	Nominal i_{corr} ($\mu\text{A cm}^{-2}$) measured from PD tests	Nominal i_{corr} ($\mu A \text{ cm}^{-2}$) measured from EIS tests
Cast	-1510 (50)	250 (20)	100 (20)	110 (15)
As-deposited	-1520 (50)	350 (50)	12 (2)	7 (1.5)

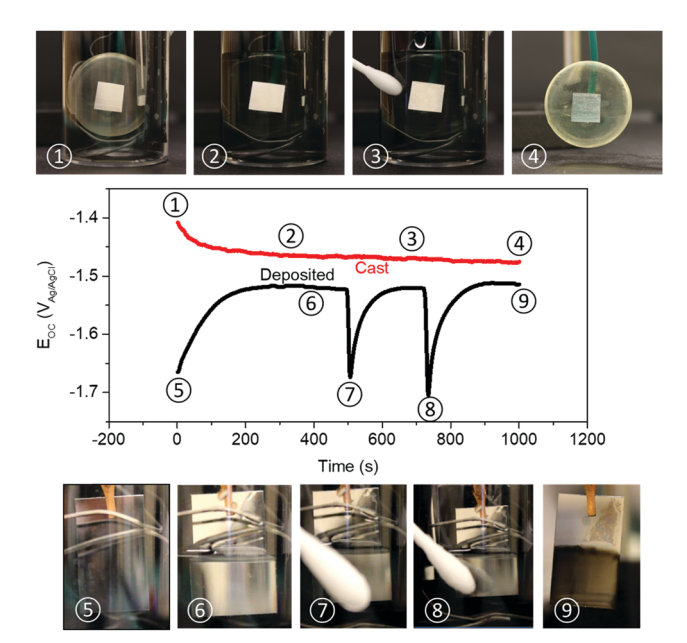


Fig. 6 Evolution of E_{OC} during the immersion test in blood bank buffered saline. A Q-tip was used to gently scrub the surface at time 2 and 3 for the cast sample, and at time 7 and 8 for the deposited sample, as labeled in the figure

Fig. 6 shows the evolution of E_{OC} for both alloys (the test was repeated for at least two samples) during immersion tests up to 15 min. It can be seen that for AD-WE43, $E_{\rm OC}$ increased from ~ -1.67 V vs. Ag/AgCl to ~ -1.52 V vs. Ag/AgCl in the first

 \sim 180 s. Such a fast increase in $E_{\rm OC}$ is often associated with passivation of the surface and formation of a protective and continuous surface film.51 In the same experiments, a cottontipped thin rod (Q-tip) was used to frequently scrub the sample surface so as to introduce a local disturbance. Such disturbance had a negligible effect on $E_{\rm OC}$ of CT-WE43. Interestingly, for AD-WE43, such disturbance led to a sudden decrease in $E_{\rm OC}$, followed by a gradual recovery once scrubbing stopped. This behavior is characteristic of a typical depassivationrepassivation behavior upon sufficient disturbance or break down of a passive film.52 Thus the presence of a somewhat protective surface layer is believed to act as a passive film and lower the anodic reaction kinetics of AD-WE43. This surface layer may consist of loosely adhering corrosion products. Upon disturbance with a soft O-tip, such an oxide layer may be fragmented and become temporarily non-protective. The relatively fast repassivation that follows quickly afterward is possibly due to an associated pH rise on the surface.⁵³ Fig. 7 shows the hydrogen evolution of both samples up to 24 h. During the entire immersion period, AD-WE43 developed fewer H₂ bubbles and sites of corrosion compared to the cast alloy, indicating a decrease in the cathodic kinetics of AD-WE43, in agreement with the PD test. The hydrogen evolution rate of CT-WE43 is ~ 0.6 ml cm⁻² h⁻¹, comparable to that reported for the same alloy elsewhere, ⁵⁴ and that of the AD-WE43 sample is ~ 0.02 ml cm⁻² h⁻¹, comparable to the values reported for magnetron sputtered Mg-Y alloys immersed in 3.5% NaCl solution at 25 $^{\circ}$ C.³⁸

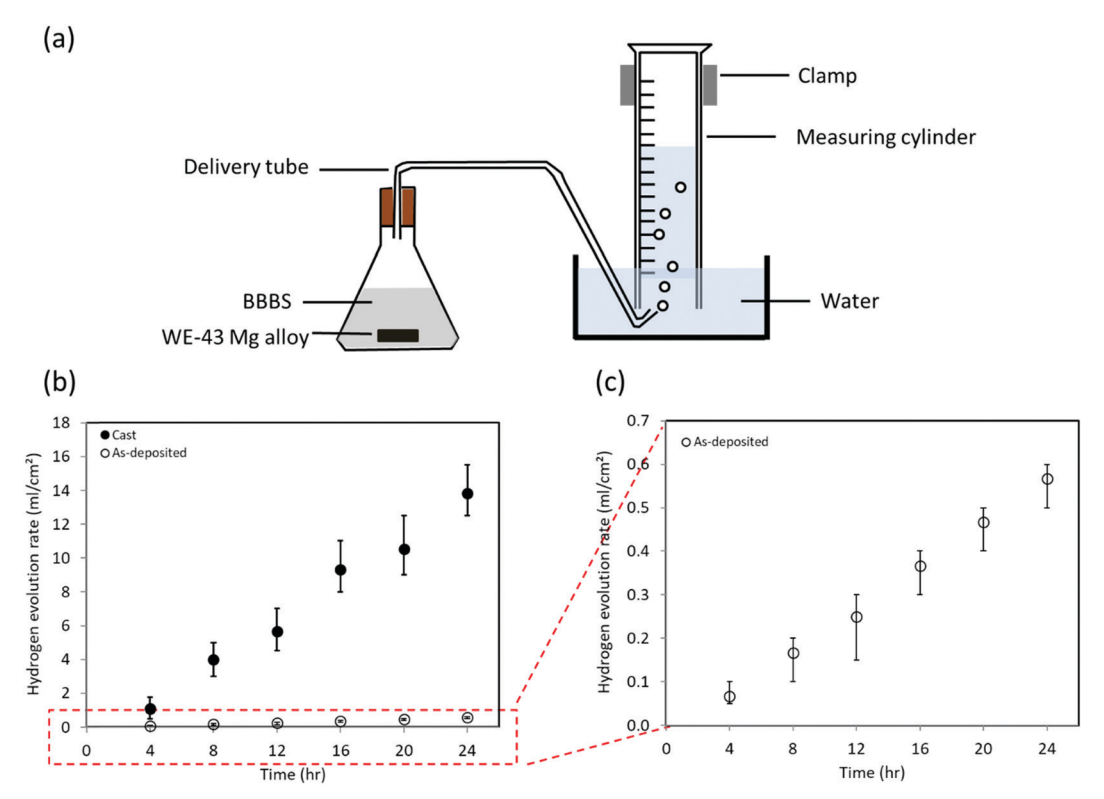


Fig. 7 (a) Schematic illustration of the hydrogen measurement setup during the immersion test. Hydrogen evolution rate of (b) both samples and (c) as-deposited WE43 taken during immersion tests of 24 h in BBBS

3.5. Nature of the surface layer

Fig. 8 shows the surface morphologies and EDS analysis of both alloys after immersion in BBBS for 4 hours. This relatively short duration of immersion was chosen to ensure AD-WE43 was not completely dissolved due to its limited thickness and high corrosion rate. The surface morphology of CT-WE43 showed a thick corrosion product film with extensive cracks, similar to that reported for the same alloy in Ringer's solution, cell culture medium and simulated body fluid.44,47 EDS maps in Fig. 8(a) show that the corrosion film on CT-WE43 was enriched in Zr and Y. In contrast, the surface of AD-WE43 was still smooth without noticeable corrosion product formation (Fig. 8(b)). The corresponding EDS maps indicated that all the alloying elements remained in solution after 4 hours of exposure. Fig. 9 shows the cross-sections of corroded samples. While CT-WE43 shows cracks $\sim 1.65 \, \mu m$ deep, AD-WE43 shows a uniform thickness (with reduced overall thickness) after the 4 h immersion test.

To characterize this surface layer, surface XPS analysis of both samples, before and after corrosion tests, was performed, as shown in Fig. 10. It can be seen that after corrosion, Mg and Y peaks shifted towards higher binding energy values for both samples, indicating that Mg and Y were oxidized to become MgO and Y₂O₃, respectively. In addition, a high P content was observed in the corroded AD-WE43, but not in CT-WE43. The observed shift in binding energy is an indication of the formation of the MgO layer on both alloys after exposure to BBBS, similar to that encountered in WE43 Mg alloys exposed to acellular SBF, cell culture medium, and Ringer's solutions with a pH range of 7.2-7.8.8,44,47,55 The presence of Y in the outermost layer of AD-WE43 before and after exposure in its metallic and oxide states, respectively, indicated that alloys produced by magnetron sputtering in this work have the advantages of not altering the global composition of WE43 Mg alloys, similar to that observed in Ti ion implanted WE43 alloys.8

To further evaluate the structure and thickness of the corrosion layer, cross-sectional TEM analysis was carried out for both alloys after immersion in BBBS for 90 min. The cross-sectional TEM sample of the corroded cast alloy was prepared by the standard FIB lift-out method. The lift-out location was selected from a representative region showing clear evidence of corrosion product formation, yet away from the cracks (Fig. 11a). To protect the surface layers from Ga ion beam

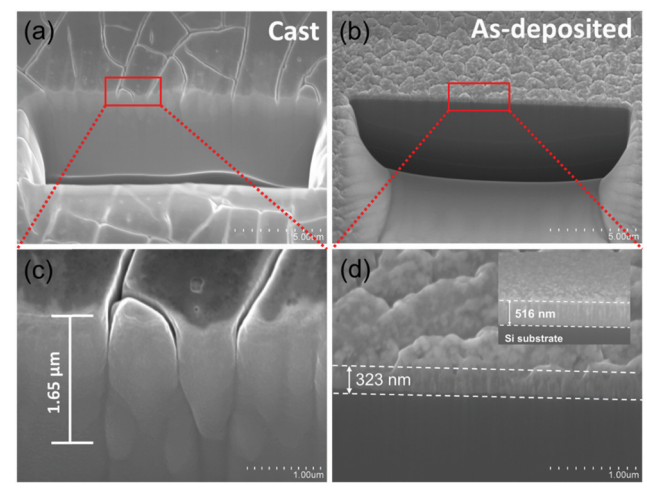


Fig. 9 Cross-sectional SEM images of the (a and c) cast and (b and d) as-deposited WE43 Mg alloy after the immersion test for 4 hours. Images (c and d) are enlarged from the boxed area in (a and b) respectively. In image (d), the bottom dark area corresponds to the Si substrate.

damage during milling, a \sim 50 nm carbon film was first deposited by e-beam evaporation followed by ion beam deposition of a Pt layer of 1–3 µm. Fig. 11(b–d) shows that a \sim 33.6 \pm 15.8 nm thick surface oxidation layer was formed on the corroded CT-WE43. To reveal the crystal nature of this layer, SAD was performed at three locations: the top (right below the surface), middle (\sim 10 nm below the surface), and bottom (\sim 15 nm below the surface), as shown in Fig. 12. The analysis of SAD patterns resulted in a lattice constant (d_{111} = 2.431 Å) that is indicative of the formation of MgO and the absence of Mg(OH)₂ in all three locations, consistent with the prior XPS results.

Cross-sectional TEM samples of the corroded AD-WE43 were prepared from an arbitrary location on the surface as no apparent corrosion product was detected on the whole surface, as indicated in Fig. 13(a). The inset in Fig. 13(a) shows that extensive grooves were formed on the surface, with an average spacing of 84 ± 15 nm, similar to the size of the surface nodules ($\sim 91 \pm 20$ nm) in Fig. 1(b). Fig. 13(b) shows that these grooves, $\sim 200-300$ nm deep and 252 ± 86 nm wide, formed preferentially along the colony boundaries. In deposited nanocrystalline metallic thin films, the presence of surface nodules has been widely reported, where the characteristic width of the surface nodule, w_c , is often orders of magnitude higher than the grain size d.

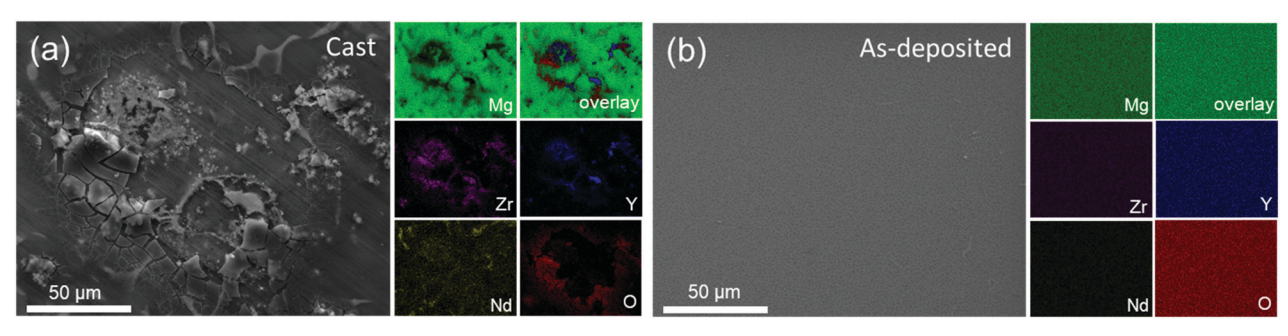


Fig. 8 Surface SEM image and the corresponding element maps of the (a) cast and (b) as-deposited WE43 Mg alloy after the immersion test for 4 hours.

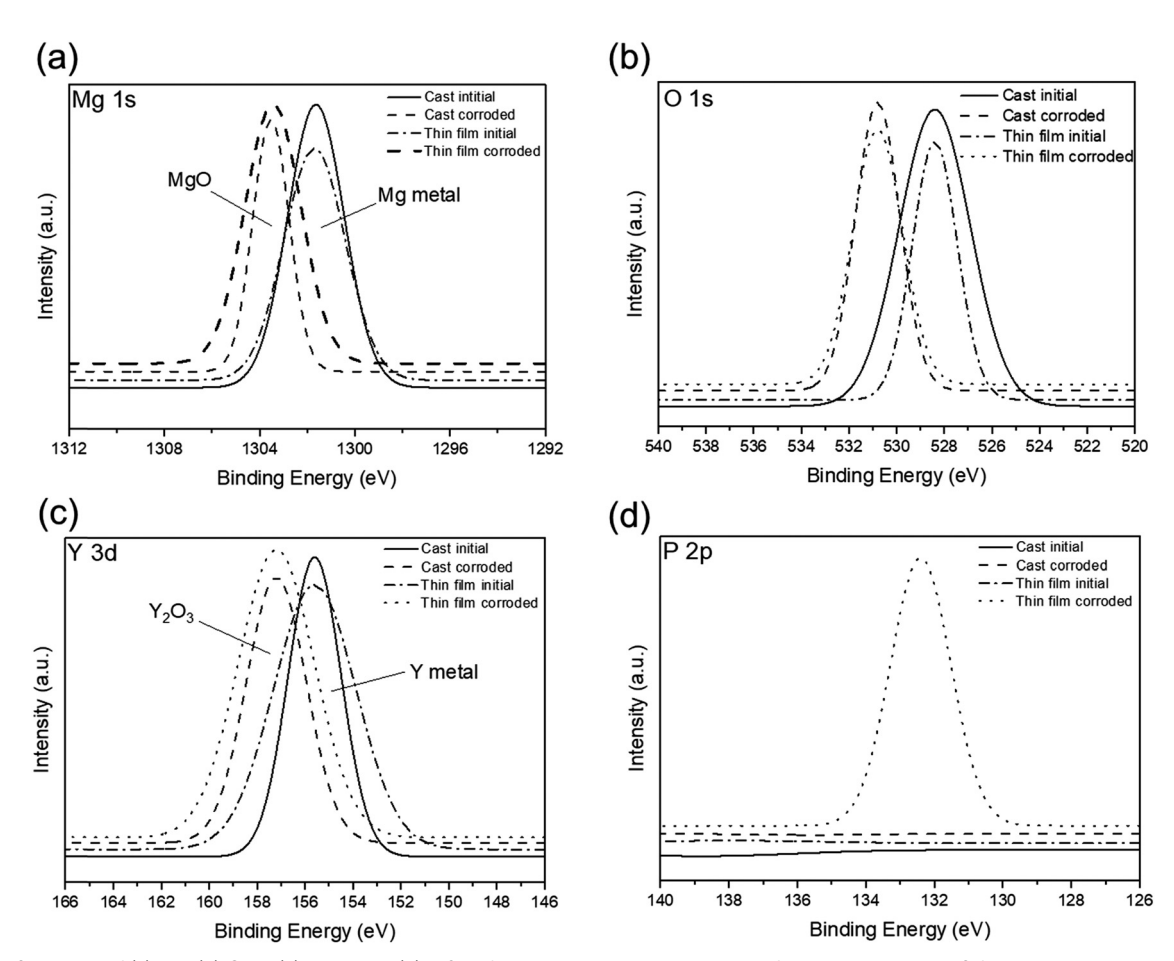


Fig. 10 XPS spectra of (a) Mq, (b) O 1s, (c) Y 3d, and (d) P 2p of cast and as-deposited alloys after exposure in BBBS for 4 h.

These colonies, which are often composed of crystallographically related grains, grow competitively during thin film growth. For example, Ruan and Schuh⁵⁶ showed that the intercolony

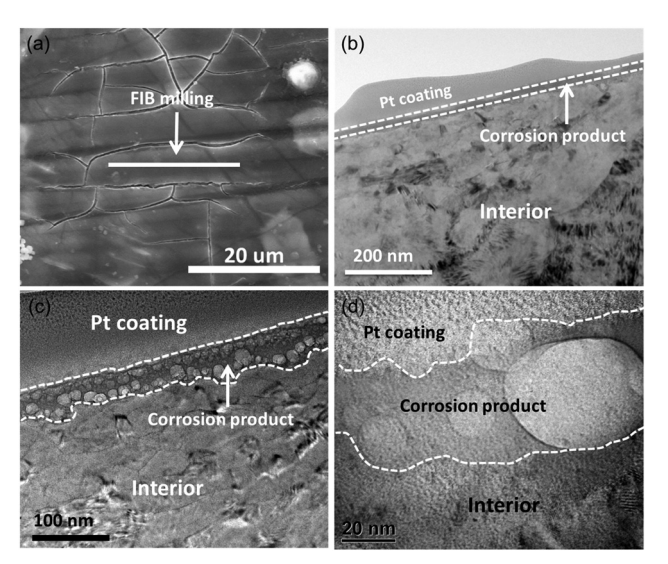


Fig. 11 (a) SEM micrographs indicating the location of FIB milling, and (b-d) TEM images at different magnifications of the cast WE43 alloy after exposure for 90 min in BBBS

boundaries of electrodeposited Ni-W are chemically and structurally different from the colony interior due to the preferred segregation of W at the boundaries, resulting in their high susceptibility to etching and cracking. In our study, a similar mechanism might also be present, resulting in preferred corrosion of the intercolony boundaries. In contrast to the cast alloy, the HRTEM image of AD-WE43 (Fig. 13(c)) did not reveal the formation of a well-defined oxidation layer of corrosion products. Instead continuous atomic planes were clearly observed from the outermost surface to the sample interior. The absence of a well-defined corrosion product layer was also revealed by the electron diffraction analysis (Fig. 13(d)), where the diffraction pattern of the outermost surface layer is formed from a crystalline Mg phase only.

The composition of the corroded surfaces of both samples was further studied by STEM-EDS analysis. Representative results are shown in Fig. 14. The corrosion product of CT-WE43 was found to have darker contrast compared to both the underneath alloy and protective layers, while AD-WE43 showed a homogeneous metal layer adjacent to the protective layer. In the corrosion product layer (~40 nm) of the corroded CT-WE43 (Fig. 14(b)), a higher O, Zr and Y content was detected, as compared to the interior. On the other hand, a well-defined oxide layer was not detected in AD-WE43 after corrosion, despite a slight increase of O content ~20 nm below the surface.

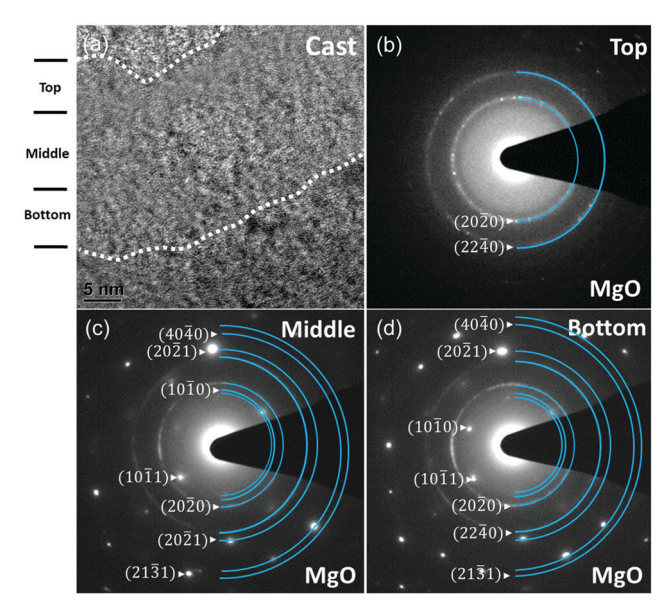


Fig. 12 (a) High resolution TEM image and (b-d) SAD of the as-cast alloy after exposure for 90 min in BBBS.

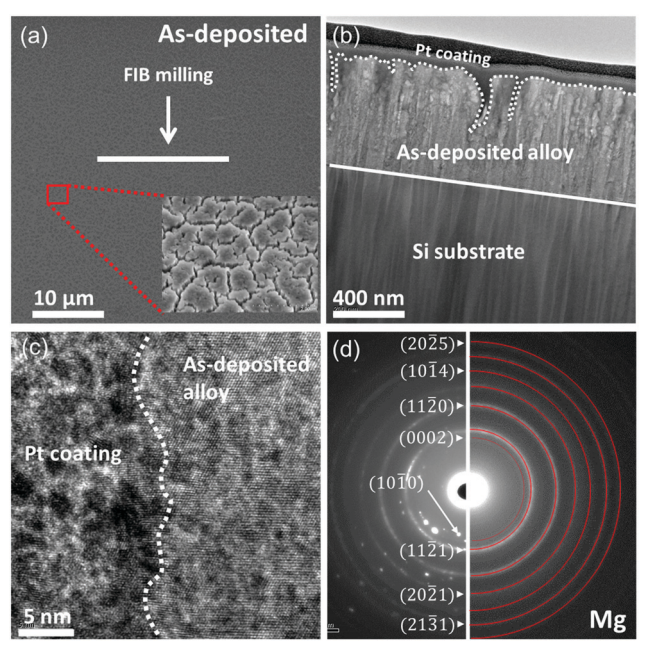


Fig. 13 (a) Surface SEM image of a corroded as-deposited sample, (b and c) TEM images and (d) SAD of the topmost surface layer of the sample after exposure for 90 min in BBBS. The inset in (a) shows a magnified SEM image of the corroded surface from the boxed area. Dashed lines in (b) and (c) represent the sample surface.

The composition, structure, and thickness of the corrosion product have a profound effect on the corrosion behavior of Mg. Yet the nature of the corrosion product formed on Mg alloys was often found to be complex and highly sensitive to pH and corrosion conditions. Typically, MgO and Mg(OH)₂ are observed in the surface films of corroded Mg alloys. For example, Taheri *et al.*⁵⁷ found that the corrosion product of commercially pure Mg exposed to water is composed of a bi-layer structure.

Other studies showed that the inner layer is rich in MgO, while the outer layer is rich in Mg(OH)₂. XPS and ToF SIMS analysis of mechanically polished Mg alloys aged in water showed that the inner layer was formed due to the reaction with oxygen gas, while the outer layer was formed due to the hydration of MgO.⁵⁸⁻⁶⁰ On the other hand, Unocic *et al.*⁶¹ found that pure Mg samples exposed to DI water for 4 hours did not show the formation of the Mg(OH)₂ layer, and this layer appeared after 24 hours of exposure. In the current study, due to the limited sample thickness of the as-deposited alloy, immersion tests were terminated after 4 h, which could explain the absence of Mg(OH)₂ on the outermost surface of both alloys.

In terms of MgO layer formation on the surface, contradictory results have been reported. For example, Nordlien et al. 62 found that an inner, dense, and amorphous MgO layer was formed naturally on a fresh Mg surface exposed to humid air and water, whereas Taheri et al.57 reported the formation of a porous and nano-crystalline MgO inner layer. Our study indicated the formation of a nanocrystalline MgO layer on the cast alloy, which is likely a result of the oxidation of Mg following the sequence oxygen chemisorption, random assembly into islands and subsequent lateral growth, oxide formation, and finally thickening. 63 Chu and Marquis⁵¹ found that for a commercial WE43 Mg alloy exposed to 3.5 wt% NaCl solution at pH ~ 10, a bi-layered corrosion product formed consisting of a porous Mg(OH)2 outer layer and a compact crystalline MgO inner layer. While prior studies offer some knowledge of surface film formation in the coarse grained WE43 Mg alloy, to the best of our knowledge, that of the nanocrystalline WE43 alloy is not yet reported. The TEM and XPS study presented in this work, coupled with disturbed $E_{\rm OC}$ measurements, indicate that a delicate, easily disrupted and self-repairing surface oxide layer is present on the as-deposited nanocrystalline alloy, which dramatically slows down the anodic reaction kinetics of Mg. The presence of this MgO surface layer was revealed by XPS and STEM-EDS line scans, although its thickness is too small to be directly measured by cross-sectional TEM analysis. The formation of this quasi-stable protective surface layer is believed to be related to the nanocrystalline nature of the thin film. Nanocrystallization has often been found to be associated with enhanced corrosion resistance in steel, Ni-based alloys, 64 and Mg alloys. 65 The small grain sizes promote uniform element distribution of alloying elements, which facilitates the rapid formation of a compact oxide layer, promotes the diffusion of passive elements in the surface layer, and reduces the adsorption of Cl⁻ on the surface. 64,66 For example, deposited nanocrystalline Mg-Ti, Mg-Cu-Y, and Mg-Ni-Nd exhibit a distinct passive region when anodically polarized in dilute chloride solution at a pH of \sim 10-12. On the other hand, the preferred corrosion of the colony boundaries of the thin film sample suggested that the dominating corrosion mechanism is the micro-galvanic coupling between the colony boundaries (anode) and the interior (cathode), likely resulting from their chemical and structural differences. Indeed, even in a non-equilibrium process such as PVD, there is still a thermodynamic driving force for the non-soluble alloying elements to segregate at grain/colony boundaries. For example, Griguceviciene et al.⁶⁸ reported the transition from a solid solution to a dual phase in PVD deposited

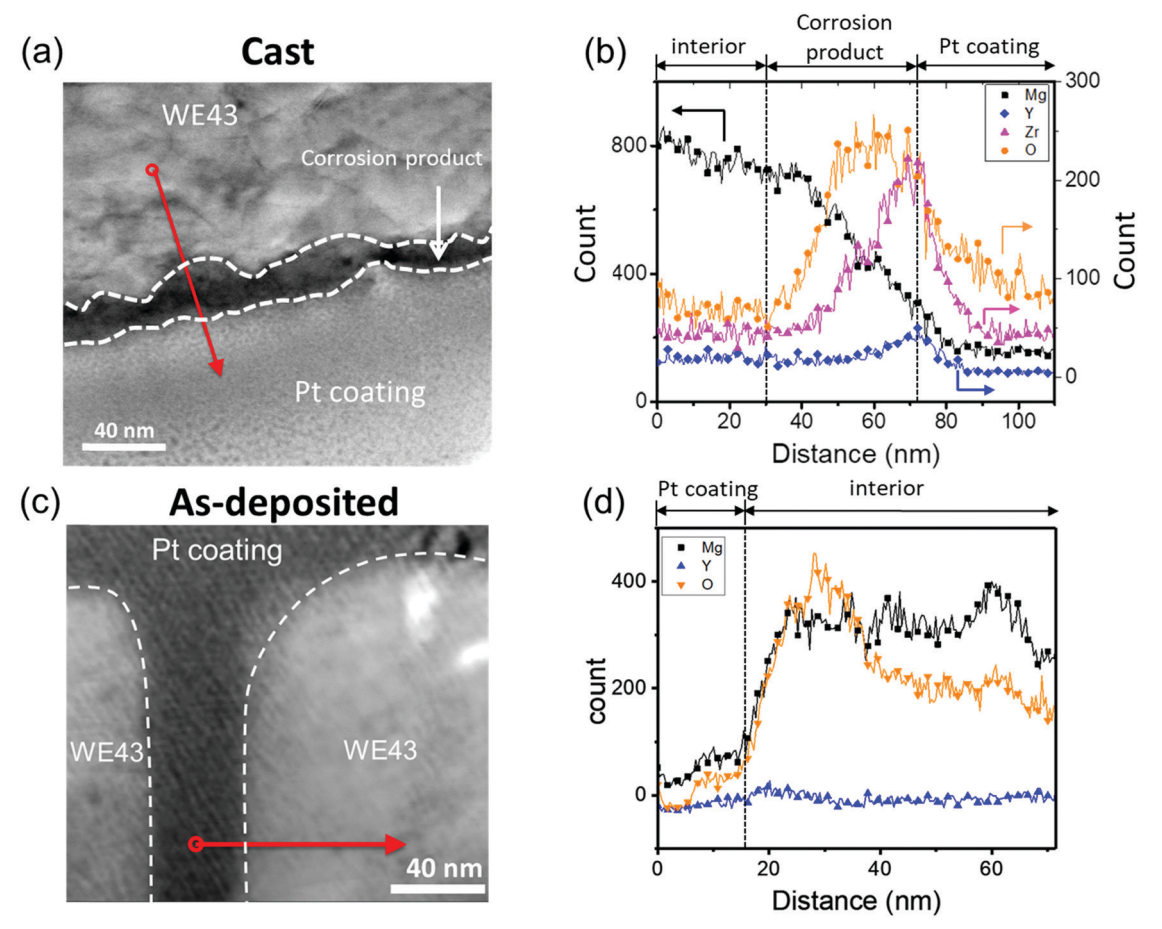


Fig. 14 (a and c) STEM image and (b and d) EDS line scan of the corrosion product after exposure for 90 min in BBBS for cast and as-deposited alloys, respectively. In images (a) and (c), the circle along the arrow represents the start (origin) of the EDS line scan.

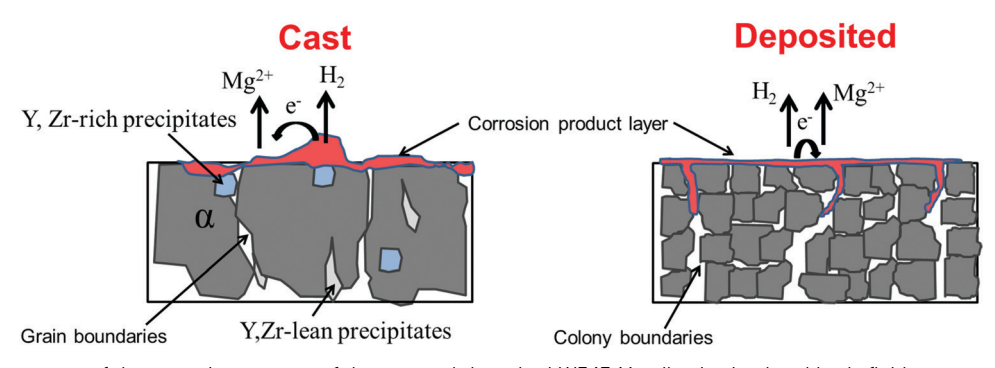


Fig. 15 Schematic summary of the corrosion process of the cast and deposited WE43 Mg alloy in simulated body fluid.

Mg-Al-Zr when Zr concentration was increased to \sim 50 at%. More detailed characterization of the chemical composition of the colony boundary can be performed using atom probe tomography, which is left for future work. Finally, Fig. 15 summarizes the corrosion mechanism of the cast and as-deposited WE43 alloy studied here. In the phase separated cast alloy, micro-galvanic coupling between the α-Mg and (Zr,Y)-rich precipitates dominates the corrosion process; a discontinuous corrosion product layer forms on the surface with a high MgO content. In the chemically homogeneous as-deposited alloy, and due to the elimination of precipitates, the dominating corrosion mechanism seemed to be the micro-galvanic coupling between the colony boundaries and the interior; the surface oxide layer is thin and delicate, but self-repairing upon local disruption.

4. Summary and conclusions

This study showed that suitable microstructure modification including minimizing precipitation and formation of a chemically

homogeneous supersaturated solid solution with an average grain size of \sim 46 nm led to a reduction of the corrosion rate of the WE43 alloy by more than one order of magnitude compared to that of the conventionally cast alloy. It is believed that minimizing precipitates led to significantly reduced cathode size and hence slowed down the cathodic reaction kinetics, while the formation of a somewhat protective surface layer on the as-deposited alloy slowed down the anodic reaction kinetics. Postcorrosion surface characterization of the cast alloy revealed that corrosion products were primarily formed above areas enriched in Zr and Y elements and exhibited a network of dehydration cracks, through which the corrosive media could penetrate towards the interior of the sample. In contrast, the as-deposited alloy managed to maintain the chemical homogeneity of the pre-corrosion condition. Corrosion was found to proceed in a more uniform fashion in the as-deposited sample due to the formation of a protective surface layer. Finally, it is understood that while physical vapor deposition is a convenient non-equilibrium processing technique to tailor alloy microstructure, it is however a surface technique and in its laboratory form not suitable for producing millimeter sized bulk samples. Nevertheless the understanding generated will provide critical design guidance for microstructure optimization in bulk samples produced by other scalable nonequilibrium techniques such as semi-solid casting, rapid solidification, cold spray, electrodeposition, powder metallurgy, etc. Such scale-up experiments and industrial development are left for future research

Conflicts of interest

There are no conflicts to declare.

Acknowledgements

This research was financially supported by the National Science Foundation under Grant DMR-1856196. The authors thankfully acknowledge the discussion of results with Kimmo Lähteenkorva and Christopher Stahle from ConMed Corporation and Dr Alberto A. Sagüés from University of South Florida. H. M. acknowledges the assistance of Nicholas G. Rudawski from the University of Florida for XPS analysis. The sample preparation and most material characterization were performed at the Nano Research and Educational Center (NREC) at the University of South Florida. XPS analysis was performed at the University of Florida.

References

R. Waksman, R. Pakala, P. K. Kuchulakanti, R. Baffour, D. Hellinga, R. Seabron, F. O. Tio, E. Wittchow, S. Hartwig, C. Harder, R. Rohde, B. Heublein, A. Andreae, K. H. Waldmann and A. Haverich, Safety and efficacy of bioabsorbable magnesium alloy stents in porcine coronary arteries, *Catheter. Cardiovasc. Interv.*, 2006, 68(4), 607–617.

- 2 B. Heublein, R. Rohde, V. Kaese, M. Niemeyer, W. Hartung and A. Haverich, Biocorrosion of magnesium alloys: a new principle in cardiovascular implant technology?, *Heart*, 2003, **89**(6), 651–656.
- 3 W. Jin, G. Wu, H. Feng, W. Wang, X. Zhang and P. K. Chu, Improvement of corrosion resistance and biocompatibility of rare-earth WE43 magnesium alloy by neodymium self-ion implantation, *Corros. Sci.*, 2015, **94**, 142–155.
- 4 F. Witte, J. Fischer, J. Nellesen, H.-A. Crostack, V. Kaese, A. Pisch, F. Beckmann and H. Windhagen, *In vitro* and *in vivo* corrosion measurements of magnesium alloys, *Biomaterials*, 2006, 27(7), 1013–1018.
- 5 C. Castellani, R. A. Lindtner, P. Hausbrandt, E. Tschegg, S. E. Stanzl-Tschegg, G. Zanoni, S. Beck and A.-M. Weinberg, Bone-implant interface strength and osseointegration: biodegradable magnesium alloy versus standard titanium control, *Acta Biomater.*, 2011, 7(1), 432–440.
- 6 A. Weiler, R. F. G. Hoffmann, A. C. Stähelin, H.-J. Helling and N. P. Südkamp, Biodegradable Implants in Sports Medicine: The Biological Base, *Arthroscopy: The Journal of Arthroscopic & Related Surgery*, 2000, 16(3), 305–321.
- 7 M. P. Staiger, A. M. Pietak, J. Huadmai and G. Dias, Magnesium and its alloys as orthopedic biomaterials: a review, *Biomaterials*, 2006, 27(9), 1728–1734.
- 8 Y. Zhao, G. Wu, Q. Lu, J. Wu, R. Xu, K. W. K. Yeung and P. K. Chu, Improved surface corrosion resistance of WE43 magnesium alloy by dual titanium and oxygen ion implantation, *Thin Solid Films*, 2013, 529, 407–411.
- 9 W. Jin, G. Wu, P. Li and P. K. Chu, Improved corrosion resistance of Mg-Y-RE alloy coated with niobium nitride, *Thin Solid Films*, 2014, **572**, 85-90.
- 10 N. Liu, J. Wang, L. Wang, Y. Wu and L. Wang, Electrochemical corrosion behavior of Mg-5Al-0.4Mn-xNd in NaCl solution, *Corros. Sci.*, 2009, 51(6), 1328-1333.
- 11 Y. Zhao, M. I. Jamesh, W. K. Li, G. Wu, C. Wang, Y. Zheng, K. W. K. Yeung and P. K. Chu, Enhanced antimicrobial properties, cytocompatibility, and corrosion resistance of plasma-modified biodegradable magnesium alloys, *Acta Biomater.*, 2014, **10**(1), 544–556.
- 12 F. Feyerabend, J. Fischer, J. Holtz, F. Witte, R. Willumeit, H. Drücker, C. Vogt and N. Hort, Evaluation of short-term effects of rare earth and other elements used in magnesium alloys on primary cells and cell lines, *Acta Biomater.*, 2010, 6(5), 1834–1842.
- 13 G. Song, Control of biodegradation of biocompatable magnesium alloys, *Corros. Sci.*, 2007, **49**(4), 1696–1701.
- 14 Y. Xin, T. Hu and P. K. Chu, *In vitro* studies of biomedical magnesium alloys in a simulated physiological environment: a review, *Acta Biomater.*, 2011, 7(4), 1452–1459.
- 15 A. Atrens, M. Liu and N. I. Zainal Abidin, Corrosion mechanism applicable to biodegradable magnesium implants, *Mater. Sci. Eng.*, *B*, 2011, **176**(20), 1609–1636.
- 16 N. T. Kirkland, G. Williams and N. Birbilis, Observations of the galvanostatic dissolution of pure magnesium, *Corros. Sci.*, 2012, **65**, 5–9.
- 17 F. Witte, V. Kaese, H. Haferkamp, E. Switzer, A. Meyer-Lindenberg, C. J. Wirth and H. Windhagen, *In vivo* corrosion

- of four magnesium alloys and the associated bone response, Biomaterials, 2005, 26(17), 3557-3563.
- 18 G. S. Frankel, A. Samaniego and N. Birbilis, Evolution of hydrogen at dissolving magnesium surfaces, Corros. Sci., 2013, 70, 104-111.
- 19 S. Thomas, N. V. Medhekar, G. S. Frankel and N. Birbilis, Corrosion mechanism and hydrogen evolution on Mg, Curr. Opin. Solid State Mater. Sci., 2015, 19(2), 85-94.
- 20 K. Gusieva, C. Davies, J. Scully and N. Birbilis, Corrosion of magnesium alloys: the role of alloying, Int. Mater. Rev., 2015, 60(3), 169-194.
- 21 Y. Ding, C. Wen, P. Hodgson and Y. Li, Effects of alloying elements on the corrosion behavior and biocompatibility of biodegradable magnesium alloys: a review, J. Mater. Chem. B, 2014, 2(14), 1912-1933.
- 22 L. L. Rokhlin, Magnesium alloys containing rare earth metals: structure and properties, CRC Press, 2003.
- 23 J. M. Seitz, R. Eifler, J. Stahl, M. Kietzmann and F. W. Bach, Characterization of MgNd2 alloy for potential applications in bioresorbable implantable devices, Acta Biomater., 2012, 8(10), 3852-3864.
- 24 Q. Wang, W. Jin, G. Wu, Y. Zhao, X. Jin, X. Hu, J. Zhou, G. Tang and P. K. Chu, Rare-earth-incorporated polymeric vector for enhanced gene delivery, Biomaterials, 2014, 35(1), 479-488.
- 25 T. Zhang, G. Meng, Y. Shao, Z. Cui and F. Wang, Corrosion of hot extrusion AZ91 magnesium alloy. Part II: effect of rare earth element neodymium (Nd) on the corrosion behavior of extruded alloy, Corros. Sci., 2011, 53(9), 2934-2942.
- 26 T. Takenaka, T. Ono, Y. Narazaki, Y. Naka and M. Kawakami, Improvement of corrosion resistance of magnesium metal by rare earth elements, Electrochim. Acta, 2007, 53(1), 117-121.
- 27 R. Arrabal, E. Matykina, A. Pardo, M. C. Merino, K. Paucar, M. Mohedano and P. Casajús, Corrosion behaviour of AZ91D and AM50 magnesium alloys with Nd and Gd additions in humid environments, Corros. Sci., 2012, 55, 351-362.
- 28 F. Witte, N. Hort, C. Vogt, S. Cohen, K. U. Kainer, R. Willumeit and F. Feyerabend, Degradable biomaterials based on magnesium corrosion, Curr. Opin. Solid State Mater. Sci., 2008, 12(5-6), 63-72.
- 29 J. Zhang, J. Wang, X. Qiu, D. Zhang, Z. Tian, X. Niu, D. Tang and J. Meng, Effect of Nd on the microstructure, mechanical properties and corrosion behavior of die-cast Mg-4Al-based alloy, J. Alloys Compd., 2008, 464(1-2), 556-564.
- 30 G. L. Song and A. Atrens, Corrosion mechanisms of magnesium alloys, Adv. Eng. Mater., 1999, 1(1), 11-33.
- 31 Y. W. Song, D. Y. Shan and E. H. Han, Pitting corrosion of a Rare Earth Mg alloy GW93, J. Mater. Sci. Technol., 2017, 33(9), 954-960.
- 32 X. B. Zhang, G. Y. Yuan, L. Mao, J. L. Niu and W. J. Ding, Biocorrosion properties of as-extruded Mg-Nd-Zn-Zr alloy compared with commercial AZ31 and WE43 alloys, Mater. Lett., 2012, 66(1), 209-211.
- 33 J. Trinidad, G. Arruebarrena, I. Marco, I. Hurtado and E. S. de Argandona, Effectivity of fluoride treatment on hydrogen and corrosion product generation in temporal implants for

- different magnesium alloys, Proc. Inst. Mech. Eng. H., 2013, 227(12), 1301-1311.
- 34 H. S. Jiang, M. Y. Zheng, X. G. Qiao, K. Wu, Q. Y. Peng, S. H. Yang, Y. H. Yuan and J. H. Luo, Microstructure and mechanical properties of WE43 magnesium alloy fabricated by direct-chill casting, Mater. Sci. Eng., A, 2017, 684, 158-164.
- 35 C. Liu, Q. Li, J. Liang, J. Zhou and L. Wang, Microstructure and corrosion behaviour of laser surface melting treated WE43 magnesium alloy, RSC Adv., 2016, 6(36), 30642-30651.
- 36 A. Mazor, D. J. Srolovitz, P. S. Hagan and B. G. Bukiet, Columnar growth in thin films, Phys. Rev. Lett., 1988, 60(5), 424-427.
- 37 T. Rzychoń and A. Kiełbus, Microstructure of WE43 casting magnesium alloys, Achiev. Mater. Manuf. Engi., 2007, 21(1),
- 38 K. Schlüter, Z. Shi, C. Zamponi, F. Cao, E. Quandt and A. Atrens, Corrosion performance and mechanical properties of sputter-deposited MgY and MgGd alloys, Corros. Sci., 2014, 78, 43-54.
- 39 C. Blawert, V. Heitmann, W. Dietzel, M. Störmer, Y. Bohne, S. Mändl and B. Rauschenbach, Corrosion properties of supersaturated magnesium alloy systems, Mater. Sci. Forum, 2007, 1679-1684.
- 40 G. Garces, M. C. Cristina, M. Torralba and P. Adeva, Texture of magnesium alloy films growth by physical vapour deposition (PVD), J. Alloys Compd., 2000, 309(1-2), 229-238.
- 41 L. G. Bland, A. D. King, N. Birbilis and J. R. Scully, Assessing the Corrosion of Commercially Pure Magnesium and Commercial AZ31B by Electrochemical Impedance, Mass-Loss, Hydrogen Collection, and Inductively Coupled Plasma Optical Emission Spectrometry Solution Analysis, Corrosion, 2015, 71(2), 128-145.
- 42 A. D. Sudholz, K. Gusieva, X. B. Chen, B. C. Muddle, M. A. Gibson and N. Birbilis, Electrochemical behaviour and corrosion of Mg-Y alloys, Corros. Sci., 2011, 53(6), 2277-2282.
- 43 N. Birbilis, G. Williams, K. Gusieva, A. Samaniego, M. A. Gibson and H. N. McMurray, Poisoning the corrosion of magnesium, Electrochem. Commun., 2013, 34, 295-298.
- 44 M. Jamesh, G. Wu, Y. Zhao and P. K. Chu, Effects of silicon plasma ion implantation on electrochemical corrosion behavior of biodegradable Mg-Y-RE Alloy, Corros. Sci., 2013, 69, 158-163.
- 45 T. Cain, L. Bland, N. Birbilis and J. Scully, A compilation of corrosion potentials for magnesium alloys, Corrosion, 2014, 70(10), 1043-1051.
- 46 E. McCafferty, Validation of corrosion rates measured by the Tafel extrapolation method, Corros. Sci., 2005, 47(12),
- 47 M. I. Jamesh, G. Wu, Y. Zhao, W. Jin, D. R. McKenzie, M. M. M. Bilek and P. K. Chu, Effects of zirconium and nitrogen plasma immersion ion implantation on the electrochemical corrosion behavior of Mg-Y-RE alloy in simulated body fluid and cell culture medium, Corros. Sci., 2014, 86, 239-251.
- 48 A. D. King, N. Birbilis and J. R. Scully, Accurate Electrochemical Measurement of Magnesium Corrosion Rates; a

- Combined Impedance, Mass-Loss and Hydrogen Collection Study, *Electrochim. Acta*, 2014, **121**, 394–406.
- 49 A. Pardo, S. Feliu Jr., M. C. Merino, R. Arrabal and E. Matykina, Electrochemical Estimation of the Corrosion Rate of Magnesium/Aluminium Alloys, *Int. J. Corros.*, 2010, 2010, 953850.
- 50 R. L. Petty, A. W. Davidson and J. Kleinberg, The Anodic Oxidation of Magnesium Metal: Evidence for the Existence of Unipositive Magnesium1,2, *J. Am. Chem. Soc.*, 1954, 76(2), 363–366.
- 51 P. W. Chu and E. A. Marquis, Linking the microstructure of a heat-treated WE43 Mg alloy with its corrosion behavior, *Corros. Sci.*, 2015, **101**, 94–104.
- 52 A. C. Vieira, L. A. Rocha, N. Papageorgiou and S. Mischler, Mechanical and electrochemical deterioration mechanisms in the tribocorrosion of Al alloys in NaCl and in NaNO₃ solutions, *Corros. Sci.*, 2012, **54**, 26–35.
- 53 R. Harrison, D. Maradze, S. Lyons, Y. F. Zheng and Y. Liu, Corrosion of magnesium and magnesium-calcium alloy in biologically-simulated environment, *Prog. Nat. Sci.: Mater. Int.*, 2014, 24(5), 539–546.
- 54 N. Li and Y. Zheng, Novel Magnesium Alloys Developed for Biomedical Application: A Review, *J. Mater. Sci. Technol.*, 2013, 29(6), 489–502.
- 55 M. I. Jamesh, G. Wu, Y. Zhao, D. R. McKenzie, M. M. M. Bilek and P. K. Chu, Electrochemical corrosion behavior of biodegradable Mg-Y-RE and Mg-Zn-Zr alloys in Ringer's solution and simulated body fluid, *Corros. Sci.*, 2015, 91, 160-184.
- 56 S. Ruan and C. A. Schuh, Mesoscale structure and segregation in electrodeposited nanocrystalline alloys, *Scr. Mater.*, 2008, 59(11), 1218–1221.
- 57 M. Taheri, R. Phillips, J. Kish and G. Botton, Analysis of the surface film formed on Mg by exposure to water using a FIB cross-section and STEM-EDS, *Corros. Sci.*, 2012, **59**, 222–228.

- 58 H. B. Yao, Y. Li and A. T. S. Wee, An XPS investigation of the oxidation/corrosion of melt-spun Mg, *Appl. Surf. Sci.*, 2000, **158**(1), 112–119.
- 59 V. Fournier, P. Marcus and I. Olefjord, Oxidation of magnesium, *Surf. Interface Anal.*, 2002, 34(1), 494–497.
- 60 A. Seyeux, M. Liu, P. Schmutz, G. Song, A. Atrens and P. Marcus, ToF-SIMS depth profile of the surface film on pure magnesium formed by immersion in pure water and the identification of magnesium hydride, *Corros. Sci.*, 2009, 51(9), 1883–1886.
- 61 K. A. Unocic, H. H. Elsentriecy, M. P. Brady, H. Meyer, G. Song, M. Fayek, R. A. Meisner and B. Davis, Transmission electron microscopy study of aqueous film formation and evolution on magnesium alloys, *J. Electrochem. Soc.*, 2014, 161(6), C302–C311.
- 62 J. H. Nordlien, S. Ono, N. Masuko and K. Nisancioglu, A TEM investigation of naturally formed oxide films on pure magnesium, *Corros. Sci.*, 1997, **39**(8), 1397–1414.
- 63 H. Namba, J. Darville and J. M. Gilles, A model for the oxidation of Mg(0001) based upon LEED, AES, ELS and work function measurements, *Surf. Sci.*, 1981, **108**(3), 446–482.
- 64 L. Liu, Y. Li and F. H. Wang, Electrochemical Corrosion Behavior of Nanocrystalline Materials – a Review, *J. Mater. Sci. Technol.*, 2010, **26**(1), 1–14.
- 65 F. Y. Cao, G. L. Song and A. Atrens, Corrosion and passivation of magnesium alloys, *Corros. Sci.*, 2016, 111, 835–845.
- 66 S. Gollapudi, Grain size distribution effects on the corrosion behaviour of materials, *Corros. Sci.*, 2012, **62**, 90–94.
- 67 G. L. Song, K. A. Unocic, M. Harry, E. Cakmak, M. P. Brady, P. E. Gannon, P. Himmer and Q. Andrews, The corrosion and passivity of sputtered Mg-Ti alloys, *Corros. Sci.*, 2016, 104, 36–46.
- 68 A. Grigucevicience, K. Leinartas, R. Juskenas and E. Juzeliunas, Structure and initial corrosion resistance of sputter deposited nanocrystalline Mg–Al–Zr alloys, *Mater. Sci. Eng.*, A, 2005, 394(1–2), 411–416.